

Electrodeposition vs Slurry Casting: How Fabrication Affects Electrochemical Reactions of Sb Electrodes in Sodium-Ion Batteries

To cite this article: Kelly Nieto et al 2022 J. Electrochem. Soc. 169 050537

View the article online for updates and enhancements.

You may also like

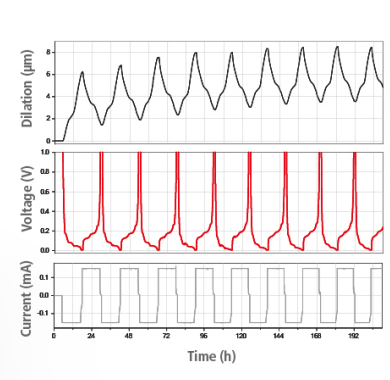
- Measurement of Volume Changes and Associated Stresses in Ge Electrodes Due to Na/Na[±] Redox Reactions Subhajit Rakshit, Akshay S. Pakhare, Olivia Ruiz et al.
- Highly Reversible Na-Ion Reaction in Nanostructured Sb₂Te₃-C Composites as Na-Ion Battery Anodes
 Ki-Hun Nam, Jeong-Hee Choi and Cheol-Min Park
- Reversible Sodium Storage Behavior of Aromatic Diimide Disodium Carboxylates
 Veerababu Medabalmi, Nirmalendu Kuanr and Kothandaraman Ramanujam

Watch Your Electrodes Breathe!

Measure the Electrode Expansion in the Nanometer Range with the ECD-4-nano.

- ✓ Battery Test Cell for Dilatometric Analysis (Expansion of Electrodes)
- ✓ Capacitive Displacement Sensor (Range 250 μm, Resolution ≤ 5 nm)
- ✓ Detect Thickness Changes of the Individual Half Cell or the Full Cell
- ✓ Additional Gas Pressure (0 to 3 bar) and Temperature Sensor (-20 to 80° C)





See Sample Test Results:



Download the Data Sheet (PDF):



Or contact us directly:

- **4** +49 40 79012-734
- www.el-cell.com





Electrodeposition vs Slurry Casting: How Fabrication Affects Electrochemical Reactions of Sb Electrodes in Sodium-Ion Batteries

Kelly Nieto, Nathan J. Gimble, Layton J. Rudolph, Amanda R. Kale, and Amy L. Prieto²

Department of Chemistry, Colorado State University, Fort Collins, Colorado 80523 United States of America

Antimony (Sb) electrodes are an ideal anode material for sodium-ion batteries, which are an attractive energy storage system to support grid-level energy storage. These anodes have high thermal stability, good rate performance, and good electronic conductivity, but there are limitations on the fundamental understanding of phases present as the material is sodiated and desodiated. Therefore, detailed investigations of the impact of the structure-property relationships on the performance of Sb electrodes are crucial for understanding how the degradation mechanisms of these electrodes can be controlled. Although significant work has gone into understanding the sodiation/desodiation mechanism of Sb-based anodes, the fabrication method, electrode composition and experimental parameters vary tremendously and there are discrepancies in the reported sodiation/desodiation reactions. Here we report the use of electrodeposition and slurry casting to fabricate Sb composite films to investigate how different fabrication techniques influence observed sodiation/desodiation reactions. We report that electrode fabrication techniques can dramatically impact the sodiation/desodiation reaction mechanism due to mechanical stability, morphology, and composition of the film. Electrodeposition has been shown to be a viable fabrication technique to process anode materials and to study reaction mechanisms at longer lengths scales without the convolution of binders and additives.

© 2022 The Electrochemical Society ("ECS"). Published on behalf of ECS by IOP Publishing Limited. [DOI: 10.1149/1945-7111/

Manuscript submitted January 3, 2022; revised manuscript received April 25, 2022. Published May 31, 2022. This paper is part of the JES Focus Issue on Women in Electrochemistry.

Supplementary material for this article is available online

Meeting the energy needs for emerging applications such as the electrification of transportation and the growing population necessitates research in alternative renewable energy and energy storage devices. Sodium-ion batteries (NIBs) are an excellent candidate for applications where weight is not a driver, such as large grid energy storage, as sodium (Na) is more naturally abundant, lower in cost, and environmentally benign when compared to popular lithium-ion batteries (LIBs). Many researchers have adapted the chemistry developed from LIBs to formulate Na analogs, but it has been discovered that not all chemistries can be transferred directly between the two systems. Commonly used anode materials such as graphite and silicon in LIBs perform poorly in NIBs as demonstrated by their very low measured capacities in NIBs. Hence, the investigation of alternative anode materials is crucial to obtain higher capacities and cycling stability in NIBs.

Antimony (Sb) is an ideal anode material in NIBs with a high theoretical capacity (660 mAh/g) and has previously been used in both LIBs and NIBs due to antimony's high thermal stability and conductivity. A major shortcoming of this alloy-type anode is the volume expansion experienced through the conversion process from Sb to Na₃Sb, resulting in issues with mechanical stability caused by the pulverization of the electrode. Also, the degradation of liquid electrolytes at the surface of Sb is not well understood. Studies have aimed to combat issues related to volume expansion and electrolyte decomposition on Sb electrodes by using the inclusion of carbon additives, ^{7–10} and different electrolyte additives. ^{11–15} Although the lifetime of Sb anodes can be extended, unanswered questions related to the understanding of structural changes during cycling of the material remain. This insight into structural changes is critical to better understand the stability, cyclability, and rate capability of Sb electrodes. While many researchers are focused on optimizing and engineering a better battery, fundamental studies on identifying structural transitions in alloy electrodes for NIBs are lacking and are crucial to the commercialization of alloy materials. There are a few reports investigating phase transitions in antimony electrodes in NIBs. Previously it was believed that the sodiation of Sb occurred by first sodiating Sb to NaSb and then the final sodiated Na₃Sb phase,

similar to the lithiation of Sb, but many reports in the literature have found that the sodiation process is much more complex. 5,14,16-25 Several studies have investigated these phase transitions and have identified various intermediate and metastable phases. 16,20,21,26,27 For example, Darwiche et al. alluded to the possible formation of cubic and hexagonal Na₃Sb as the final sodiated phase using in situ X-ray diffraction and Allan et al. was able to identify two sodiated amorphous phases, Na_{3-x}Sb and Na_{1.7}Sb, using pair distribution function analysis and solid-state NMR spectroscopy. 5,20 In addition Lee et al. has predicted the possibility of a multitude of metastable intermediate phases forming under commonly used battery cycling conditions. 26

Although these studies have made significant contributions to the fundamental understanding of the reaction pathway of antimony in Naion systems it is hard to compare results obtained between the different studies. The Sb electrodes in these studies are fabricated with different techniques and are cycled using different electrolytes and experimental parameters that can influence the reaction pathway. 5,20 Typically the slurry casting method is utilized to fabricate electrodes and uses different polymeric binders and conductive additives that have been shown to influence electrochemical performance for various reasons such as mechanical stability, excessive SEI formation and the ability for components other than Sb to reversibly sodiate.²⁸⁻³³ Other studies investigating Sb electrodes use different additives or even different fabrication techniques, such as sputtering and electrodeposition. ^{25,34} By comparing the data presented in all these studies that are investigating antimony electrodes, it is apparent that electrode fabrication, electrolytes, and different cycling parameters may be causing significant differences in the electrochemical reactions present. 5,20,2

Previously our group has used electrodeposition to form anode films that enables the direct deposition of active material onto a metal foil current collector without the use of additives or binders like that of slurry casted films. ^{7,36–40} This technique allows for the investigation of the intrinsic properties of the active material without the need to deconvolute data from the active material and inactive binders. Electrodeposition also allows for the co-deposition of antimony with conductive material such as amine functionalized carbon nanotubes (ACNTs) to extend cycle life. Schulze et al., created a co-deposition procedure for the deposition of antimony thin films on textured copper foil with an ACNT network for Li-ion

cells.³⁴ It was found that ACNTs extend cycle lifetime by maintaining electronic conductivity within the Sb film even when cracking due to volume expansion occurs.³⁴ This mechanical stability allows for Sb/ACNT to act as the model anode and would allow for the study of the sodiation/desodiation pathway at longer cycle lifetimes.

Here we report the use of two fabrication techniques, slurry casting and electrodeposition, to investigate how differences introduced from electrode fabrication, such as composition and morphology, impact the electrochemical reactions occurring as Sb anodes are cycled in NIBs. We used differential capacity analysis (DCA) to compare the electrochemical performance and reaction mechanism of electrodeposited and slurry casted composite films. The inclusion of electrochemically active binders and conductive additives that sodiate inhibit understanding of the reaction mechanism. In contrast, electrodeposited Sb films allow for a better understanding of the mechanism as this method was found to allow significant control of composition, morphology, and mechanical integrity of Sb anodes. Through electrodeposition, we demonstrate a feasible technique to study the intrinsic properties of Sb and its sodiation/desodiation reaction mechanism and degradation. By understanding these fundamental processes and developing the tools and characterization techniques to study alloy-based anode materials, these studies will accelerate the understanding and processibility of anodes for energy storage applications.

Experimental

Electrodeposition solution of Sb and Sb/ACNT.—The electrodeposition solution of Sb and Sb/ACNT were both composed of 200 mM sodium gluconate (Sigma, ACS reagent), 30 mM of antimony trichloride (SbCl₃, Sigma-Aldrich, anhydrous >99.0%) and 30 mM of cetyl trimethyl ammonium bromide (CTAB, Alfa Aesar 98%). The Sb/ACNT solution additionally had 200 mg of ACNTs (Cheap Tubes, outer diameter 20 nm, inside diameter 4 nm, and length from 1–12 μm, >99 wt% purity).

In both electrodeposition solutions, sodium gluconate was stirred in a beaker containing 100 ml of Millipore (>15 $M\Omega^*cm)$ water for $\sim\!5$ min. Then $SbCl_3$ was added to the solution and sonicated (VWR Model 50 HT) until a homogeneous mixture was formed. The pure Sb solution was then complete and CTAB was added to the beaker containing the Sb and gluconate solution intended for the Sb/ACNT deposition. The solution was sonicated until clear and mostly colorless. The Sb/ACNT solution was returned to a stir plate in a hood and 200 mg of ACNTs were added. The solution was pulse sonicated for two hours with a 10 min pulse and 2 min rest sequence.. The excess ACNTs were then crashed out through centrifugation. The solution was split evenly into two 50 ml centrifuge tubes and was centrifuged for 5 min at 5000 rpm. The supernatant was decanted and the excess ACNTs were saved for later use.

Electrodeposition solution of ACNTs.—The procedure for the ACNT deposition solution was similar to that of the Sb/ACNT

without the use of antimony. The solution was composed of 100 ml of Millipore water, 200 mM sodium gluconate, 30 mM of CTAB, and an excess of ACNT consisting of 1 heaping scoopula of ACNT for every 20 ml of solution. All sonication and centrifugation procedures used for the Sb/ACNT solution were followed.

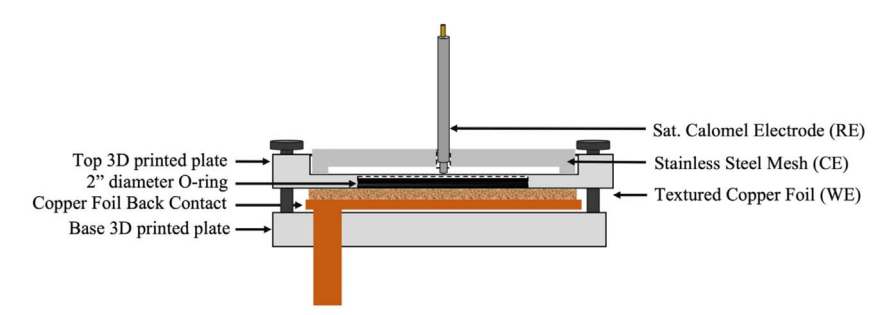
Electrochemical characterization of deposition solutions.—Cyclic voltammetry (CV) was used to characterize the deposition solutions and determine the reduction potential at which to deposit Sb. A Gamry Reference 3000 potentiostat was used to perform these experiments. The CVs were taken in a three-electrode set up consisting of a saturated calomel electrode as the reference, a platinum counter electrode, and a platinum disk working electrode at a scan rate of 50 mV s⁻¹ unless otherwise noted.

Electrodeposition of Sb@tCu and Sb/ACNT@tCu.—The thin film electrodes were electrodeposited using a Gamry Interface 1010E potentiostat and the apparatus pictured in Fig. 1. A fourinch square of textured Cu foil (tCu, Oak-Mitsui, TLB-DS Cu foil) was washed with a concentrated H₃PO₄ solution for 30 s to remove oxides on the surface, followed by Millipore water and ethanol wash to remove excess acid and water on the surface of the film. The clean film was placed in the apparatus pictured in Fig. 1. Approximately 100 ml of the Sb or Sb/ACNT deposition solution were used to cover the tCu and the stainless-steel (SS) mesh. The saturated calomel electrode (SCE) was placed through an opening in the SS mesh to lessen the distance between the textured copper foil and the SCE to reduce the measured resistance in the system. Using chronocoulometry a constant negative potential of -1.05 V vs SCE was applied to the system and the charge limit was set to 3 C cm⁻². When the deposition was complete, the deposited area was washed with Millipore water and absolute ethanol and was dried with nitrogen

Electrophoretic deposition of ACNTs.—A constant negative potential of -1.05 V vs SCE was applied to the system and the charge limit was set to 3 C cm $^{-2}$. The deposition was run for \sim 1 h, similar to the time it took to complete the Sb/ACNT deposition.

Preparation of slurry casted films.—The slurry composites consisted of active material, a conductive additive, and a binder at a ratio of 70:15:15 wt%. The composites were doctor bladed onto textured copper foil at a thickness of 150 μ m. After casting the films were dried with specific drying procedures depending on the wetting solvent used.

Sodium carboxymethyl cellulose (CMC, Aldrich, DS = 0.7, $M_{\rm w}=250,\!000$) was first dissolved in 2.5 ml of Millipore water in a vial at 80 °C while stirred. The CMC suspension was allowed to stir for one hour or until the powder was completely dissolved and the solution was viscous. Sb powder (~200 mesh, Alfa Aesar, 99.5%), and carbon black (Super P conductive, Alfa Aesar >99%) were ball milled for one hour in a Fritsch planetary ball mill at 650 rpm. The ball milled powder was then added in batches to the CMC solution and was stirred for 30 min for each batch. Textured copper foil (tCu, Oak-Mitsui, TLB-DS Cu foil)



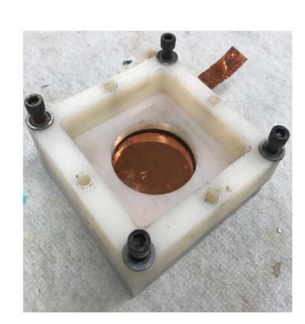


Figure 1. Apparatus designed and used for the electrodeposition of Sb/ACNT where the copper foil back contact acts as the working electrode, a stainless-steel mesh acts as the counter electrode, and a saturated calomel electrode is used as the reference electrode.

was then smoothed out on a glass panel with ethanol to prevent the doctor blade from catching on creases in the foil. The doctor blade was then used to cast a 150 μ m thick film. The film was dried for 12 h at room temperature and then dried in a vacuum oven at 80 °C overnight.

The binder poly(acrylic acid) (PAA, Sigma-Aldrich, $M_v = 450,000$) was dissolved in 2.5 ml of 1-methyl-2-pyrrolidinone (NMP, Sigma-Aldrich, ACS reagent, $\geqslant 99.0\%$,) in a vial at room temperature while stirred. The PAA suspension was allowed to stir for one hour or until the powder was completely dissolved and the solution was viscous. Sb powder and Super P were ball milled for one hour at 30 Hz in a Retsch Cryomill. The ball milled powder was then added in batches to the PAA solution and was stirred for 30 min for each batch. The films were casted using the same procedure mentioned for the CMC based slurries. These films were dried in a vacuum oven overnight at 80 °C.

All slurry controls were casted using the procedures described above. The Super P control was casted at a 50:50 wt% ratio of Super P to PAA. The PAA and CMC controls were casted using only the binder in question using the solution preparation described above to dissolve the binders in their respective wetting solvents.

Electrolyte preparation, cell assembly, and galvanostatic cycling.—All tested electrolyte solutions were made in an argon glovebox. The electrolyte used for all experiments consisted of a 1 M solution of sodium perchlorate (NaClO₄, Sigma-Aldrich, ≥98% ACS reagent) with an addition of 5% by volume fluoroethylene carbonate (FEC, Sigma-Aldrich, 99%) in a base electrolyte solution containing polyethylene carbonate (PC, Sigma-Aldrich, 99.7%).

All half-cells were assembled in two electrode Swageloks, in an argon filled glove box. The electrodeposited film was cut into circular $\frac{1}{2}$ " in diameter punches and were weighed out to acquire the mass of the active material. The thin films were used as the working electrode and a polypropylene separator (MTI Corp) followed by a Whatman glass filter, and another polypropylene separator were used to prevent shorting through anode and cathode contact. An excess amount of electrolyte, \sim 0.20 μ l, was placed in the cell after the separators. Na metal (Aldrich, cubes in mineral oil, 99.9%) was then rolled out with a Teflon roller with hexanes, cleaned with an extra soft child's toothbrush and was punched into a $\frac{1}{2}$ " circular punch. Pressure was then applied through the spring to the SS rod and the Cu rod to make sure that all parts were in contact in the Swagelok.

Once assembled, the Na-ion half-cells were cycled with an Arbin battery tester (LBT-20084). The cells were allowed to rest for 12 h after assembly and were galvanostatically cycled at 0.1 mA mg⁻¹ with calculated current densities based on the mass of active material in the deposited thin films. The voltage range at which the cells were cycled was 0.01 V to 2.0 V vs Na⁺/Na unless otherwise noted. Cycling performance was analyzed and graphed with Python code using the NumPy and Pandas packages.

Materials characterization.—The surface morphology of electrodeposited and slurry casted films was analyzed with Scanning Electron Microscopy (SEM) using a JEOL JSM-6500F Microscope at 15 kV, Energy Dispersive X-ray Spectroscopy (EDS) with an Oxford Instrument X-Max and AZtec software. X-ray Photoelectron Spectroscopy (XPS) was performed using a Physical Electronics (PHI) 5800 series Multi-Technique ESCA system with a monochromatic Al $K\alpha$ (hν = 1486.6 eV) X-ray source operating at 350.0 W. Further structural characterization was done with Powder X-ray Diffraction (PXRD) with a Bruker D8 Discover DaVinci powder X-ray diffractometer using Cu $K\alpha$ radiation.

Results and Discussion

Electrodeposition of Sb@tCu and Sb/ACNT@tCu Composite Films.—Thin films of Sb@tCu and Sb/ACNT@tCu were synthesized through electrodeposition using a solution containing SbCl₃, CTAB, sodium gluconate, and ACNT. To maintain the solubility of Sb³⁺ in solution, sodium gluconate has previously been reported to

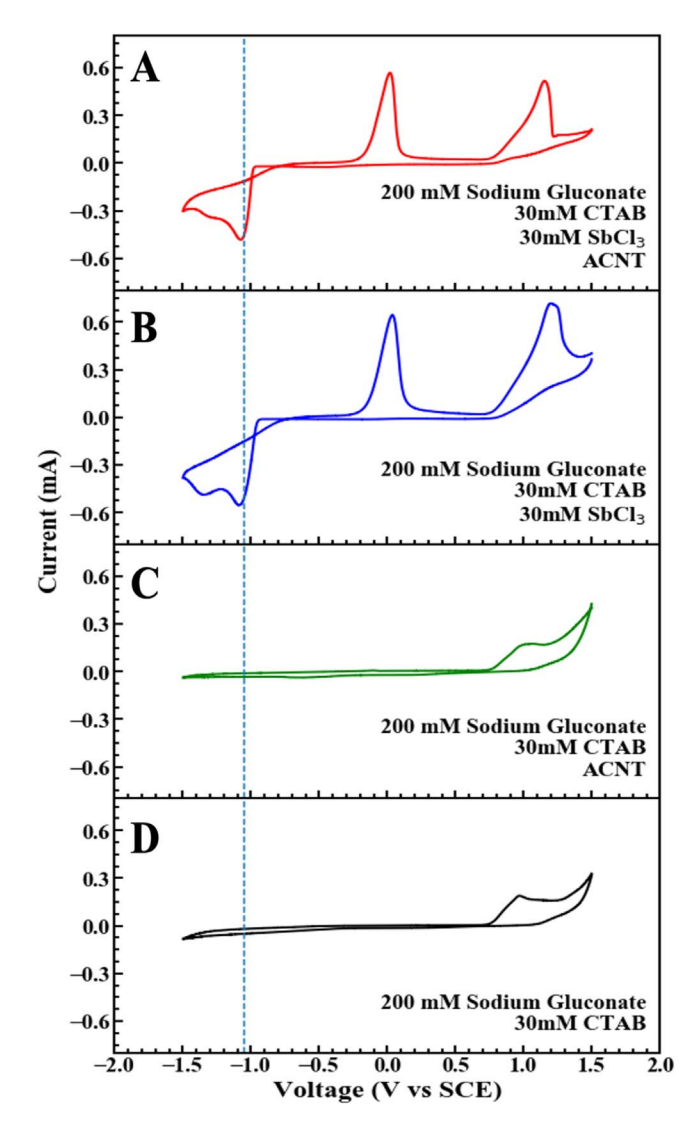


Figure 2. Cyclic voltammograms of individual components of the electrodeposition solution for both Sb and Sb/ACNTs. A scan rate of 50 mV s⁻¹ was used, and the potential was swept to negative potentials then positive potentials. The blue dashed line represents the reduction potential of Sb³⁺ + $3e^- \rightarrow Sb^0$ vs SCE.

complex with Sb^{3+} in solution to prevent the precipitation of antimony oxide species. ⁴¹ Additionally, CTAB acts as the cationic surfactant that aids in the suspension of ACNT in solution. 34,42 In order to find the potential at which Sb should be deposited, CVs of the electrodeposition solution and its individual components were collected. The cyclic voltammogram of the electrodeposition solution revealed two reduction events and two oxidation events as presented in Fig. 2. The reduction peak seen at -1.05 V vs SCE when sweeping in the cathodic direction is representative of the reduction of Sb³⁺ to Sb⁰. In the reverse direction, the oxidative event at 0.0 V represents the oxidation of Sb⁰ to Sb³⁺ as this event was not present without the use of SbCl₃ in the solution. The second oxidative event at +1.05 V represents an irreversible oxidation reaction occurring when CTAB and sodium gluconate are in solution. From these results, the electrodeposition of Sb and Sb/ ACNT was conducted at the negative reduction potential of -1.05 Vto ensure that only Sb3+ was being reduced onto the negatively biased textured Cu foil.

Characterization using SEM, EDS, and PXRD was performed to investigate the composition, uniformity of the film, and to confirm that ACNTs were incorporated in the deposition. The Sb was reduced onto the foil in densely-packed, spherically-shaped particles

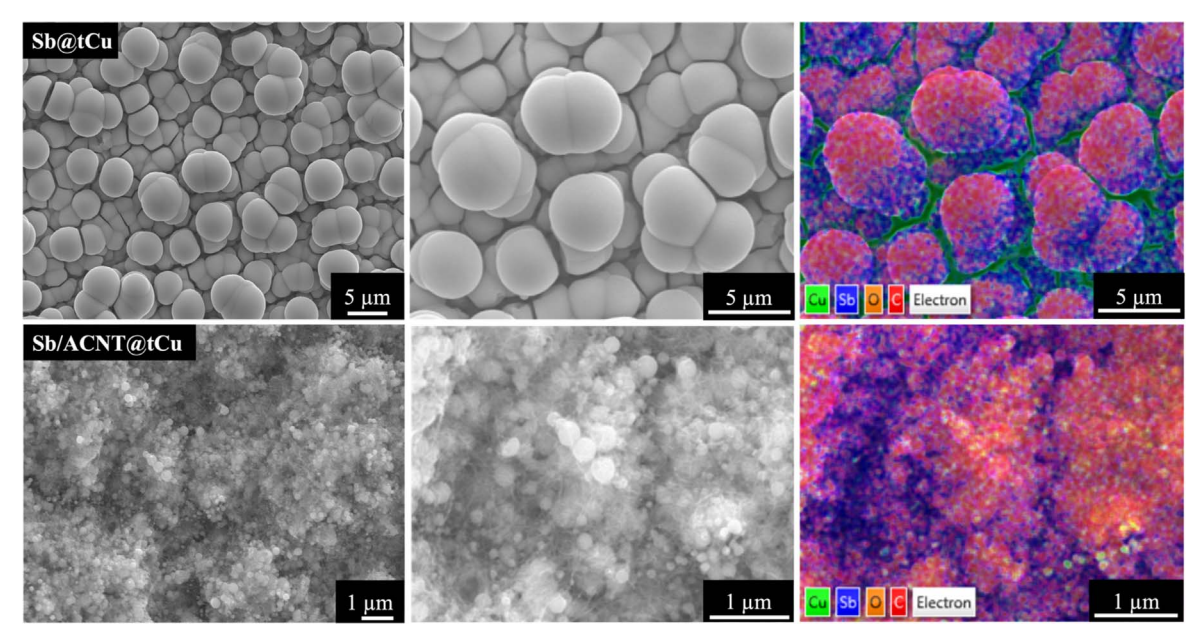


Figure 3. SEM and EDS of Sb@tCu and Sb/ACNT@tCu.

as seen in Fig. 3. In the Sb/ACNT@tCu film, Sb was reduced onto the ACNTs as seen by the nodular growth of Sb onto the ACNTs through SEM and EDS, Fig. 3, and creates a porous film that in turn increases surface area and increases the number of oxides and SEI build up upon cycling.³⁴ In addition to the increased porosity of the Sb/ACNT@tCu film, the thickness also increases from 5.34 μ m for the Sb@tCu film to 7.55 μ m. These thicknesses were calculated from cross-section SEM images seen in Figs. S1 and S2 (available online at stacks.iop.org/JES/169/050537/mmedia). The Sb particle size between electrodes decreased from approximately 5 μ m in the Sb@tCu films to 100 nm in the Sb/ACNT@tCu. During the coelectrodeposition of Sb with ACNTs, ACNTs are directly deposited on the copper foil as well as on Sb particles that have already plated. We believe the inclusion of ACNTs introduces a wider distribution of nucleation sites due to the increase in surface area after the ACNTs have electrophoretically deposited on the copper foil. This change in particle size is expected to affect the rate capabilities of the Sb anode due to Na⁺ diffusion and is not investigated in this report. ³⁴ By analyzing the EDS, shown in Fig. 3, we observe that the majority of the film's surface is made up of Sb and/or Sb with ACNTs. Significant oxygen inclusion can be attributed to the oxidation of the film's surface to form Sb₂O₃. PXRD patterns of both Sb@tCu and Sb/ACNT@tCu films, Fig. 4, show that the films are Sb of low crystallinity, as indicated by the broad reflection at 29° 2θ . All peaks can be assigned to Sb or the Cu substrate (Fig. S3), and no crystalline oxides are observed, which suggests that the oxides are primarily on the surface or are amorphous. The broad peak can be assigned to the Sb [102], and given that strain in electrodeposited films made at room temperature is common, we suspect that the breadth of this peak is partially due to strain in the film along this direction. The right shift of this peak relative to the slurry casted Sb films (discussed below) suggests a smaller unit cell for electrodeposited films, which is consistent with more densely packed Sb that may be strained (Fig. S4).⁷

The low crystallinity is potentially significant because the formation of crystalline or amorphous Sb anodes for NIBs was previously investigated by Yang et al. and it was concluded that after the first cycle Sb remains amorphous.³⁵ In addition, Allan et al. found that the starting crystalline anode can have implications on the sodiation pathway in the first cycle caused by the shift to overpotentials to break down the crystalline Sb.²⁰ These discrepancies between amorphous and crystalline anodes were taken into account in the work reported herein, and mechanistic studies were conducted

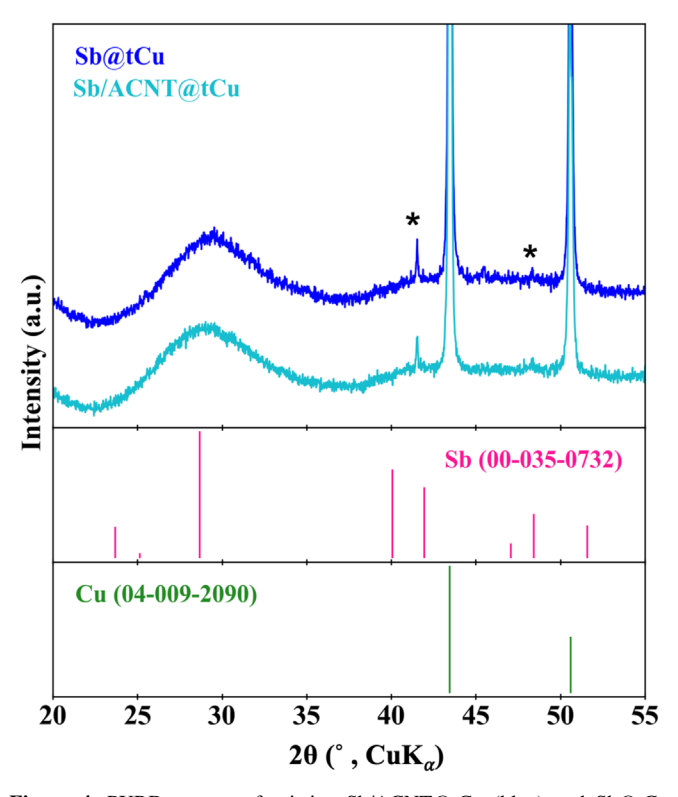


Figure 4. PXRD pattern of pristine Sb/ACNT@tCu (blue) and Sb@tCu (cyan). Peaks denoted by asterisks are observed in the PXRD pattern for textured copper foil shown in Fig. S3.

over longer cycle numbers to overcome the large shifts in reaction potentials in the first two cycles.

Electrochemical performance of electrodeposited Sb@tCu Sb/ACNT@tCu in Na-ion half-cells.—The electrochemical performance of Sb@tCu and Sb/ACNT@tCu in a Na-ion half-cell was first investigated through galvanostatic cycling in a Swagelok with 1 M NaClO₄ in PC with 5% FEC as the electrolyte. The cycle lifetime and the capacity retention of the electrodeposited films Sb@tCu and Sb/ACNT are shown in Fig. 5. In the first cycle, a

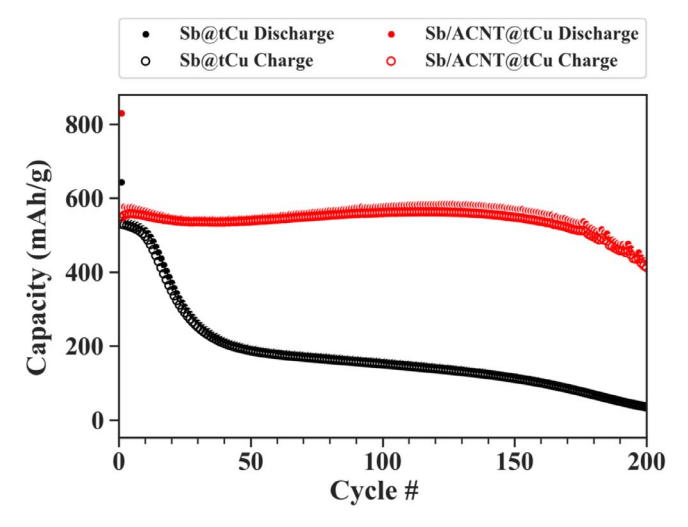


Figure 5. Specific Capacity of Sb@tCu and Sb/ACNT@tCu in Na-ion half-cells cycled at $0.1~\rm{mA~mg}^{-1}$.

significant amount of capacity is lost as it is believed that the first cycle mainly involves the formation of the solid electrolyte interphase (SEI).³⁷ Initially the SEI may serve as a protective layer, but in later cycles leads to capacity fade as the layer is electronically insulating and traps and Na ions, preventing them from entering the anode.⁶ Both Sb@tCu and Sb/ACNT@tCu show stable cycling until 50 cycles after which the capacity for the Sb@tCu film quickly diminishes demonstrating how the inclusion of ACNTs has significantly extended the cycle life. This extension in lifetime is crucial for commercialization but also allows for monitoring of significant changes of the electrochemical reactions occurring over time that may provide insight into degradation pathways.

To further compare the performance of Sb@tCu to Sb/ ACNT@tCu, differential capacity analysis (DCA) was used to gather information about the sodiation and desodiation events occurring over a potential range. DCA plots represent a fingerprint that highlights cell degradation, failure mechanisms, and changes in chemistry that otherwise might not be seen in a voltage profile or cycle lifetime plots. 43 In Fig. 6, four significant sodiation and three desodiation events are present. The number of processes demonstrate complex multistep reactions and intermediate formation that agree with previous studies that focused on the reaction mechanism of Sbbased anodes. 20,25,26 Most studies in the literature show discrepancies between the number of sodiation/desodiation reactions, and assignment of side reactions, with little agreement. Despite these discrepancies, we have postulated the identity and progression of these reactions occurring based on studies closely related to our experimental parameters (Table I). Through the DCA plots, it is noted that over time the electrochemical reactions decrease in intensity and begin shifting to overpotentials. The decrease in intensity of the reactions is due to the loss of active material arising from the volume expansion that Sb-based electrodes experience. In the Sb@tCu film, the diminishing of the peaks occurs much sooner in comparison to the Sb/ACNT@tCu film, and with fewer shifts to overpotentials suggesting pulverization and delamination of the film to be the degradation mechanism. Although ACNTs help extend the lifetime by maintaining electronic conductivity and the integrity of the film, more SEI is formed as a result of the increased surface area from the porous nature of the film seen in Fig. 3. This increase in SEI formation leads to overpotentials caused by kinetic limitations induced by the continuous formation of SEI over many cycles and is suggested to be the main failure mode of Sb/ACNT@tCu films. 34 Electrolyte optimization and its influences on the kinetics of the electrochemical reactions present will be investigated in later studies.

Taking a closer look at the DCA, a small broad peak can be seen in the sodiation at 1.0 V vs Na/Na⁺ in cycle one and is attributed to

the conversion of Sb₂O₃ to Sb. Oxides were shown to be included in the film and its impact on the electrochemical reactions of Sb will be discussed in detail in later sections. The following reaction, peak "a", is known to be the initial conversion and sodiation of Sb to Na_xSb (0<x≤1) followed by the continuous sodiation of the amorphous intermediate to various Na_vSb (1<y<3) phases over the potential ranges of 0.70–0.50 V vs Na/Na⁺ in peak "b". Through ²³Na MAS ssNMR and PDF analysis Allan et al. have been able to identify these reactions as the sodiation of Sb to form Na_{1.7}Sb and $Na_{3-x}Sb$ (0.4 < x < 0.5), and these reactions will be referenced to these studies moving forward.²⁰ Although these reactions have been identified in their system (slurry casted Sb:CMC:Super P) small discrepancies may be present due to the lack of crystallinity of our starting Sb film, the lack of binders present in our system, and the electrolyte used. Note that the kinetics of the sodiation of Sb are governed by crystalline and amorphous domains present after full desodiation as well as the influences of SEI formation. Future studies will focus on comparing the identity of these reactions for electrodeposited films and other studies in the field using slurry casted composites.

The sodiation of the Na_{3-x}Sb phase is continued and begins to form the final hexagonal Na₃Sb phase in peak "c" and possibly the formation of the high pressure metastable cubic Na₃Sb phase. The metastable Na₃Sb cubic has been seen in very small quantities in previous reports and has been synthesized through solid state methods at high pressures of 10^{-4} –9.0 GPa. 5,16,44,45 We postulate that the formation of the metastable phase may be occurring due to the dense packing of Sb particles (or strain in the film). As mentioned above, the broad peak observed in PXRD would be consistent with a film that was strained prior to cycling. As the majority of the particles begin to sodiate to the final Na₃Sb phase, the internal pressure of the film begins to rise, caused by the particles further pushing against each other, which is induced by the volume expansion of the active material. We plan to test this hypothesis in future studies through pressure testing, modeling, and beamline in situ XRD experiments. The final sodiation peak "d" is not always present in Sb anode reports and at times is ignored because of the low peak intensity. In our electrodeposited films, the final sodiation reaction is readily present and we hypothesize this reaction to be the continued formation of the final sodiated hexagonal Na₃Sb phase, and the formation of the metastable Na₃Sb cubic phase at overpotentials. Peak "d" begins to increase in intensity when peak "c" decreases in intensity and elucidates that peaks "c" and "d" are similar sodiation reactions. These limitations possibly occur due to kinetic limitations in nucleating crystalline Na₃Sb when Sb-Sb bonds are still present therefore shifting the reaction to overpotentials.²⁰ Other factors, such as increased surface area and SEI formation, may be causing limitations in Na⁺ diffusivity as seen in Fig. 6 when comparing peaks "c" and "d" in the Sb@tCu and Sb/ACNT@tCu systems. The Sb/ACNT@tCu systems has a larger surface area because of the inclusion of the ACNTs as discussed previously and can be seen when comparing the SEM in Fig. 3. This increased surface are leads to greater SEI formation and the shift to overpotentials for peak "c" occurs sooner as demonstrated by the decline in intensity of the peak in earlier cycles when compared to the Sb@tCu system.

The desodiation process begins with the desodiation of the cubic and hexagonal Na_3Sb phases to $Na_{1.7}Sb$ and some remaining crystalline Na_3Sb in reaction "e". At 0.77~V vs Na/Na^+ , the majority of the film has been desodiated and mainly consists of $Na_{1.0}Sb$ where the desodiation of Sb is believed to be a more spontaneous process than the sodiation and attributes to less distinct processes. These broader peaks have been observed in other studies and have been associated to better Na^+ diffusion in the Na_3Sb phase, but then the desodiation of this phase is thought to be kinetically limited in reforming crystalline $Sb.^{20}$ The final desodiation step is hypothesized to be the conversion of $Na_{1.0}Sb$ to amorphous Sb but may remain mostly as $Na_{1.0}Sb$ as other studies have shown that the reformation of crystalline Sb is kinetically limited. $Sb.^{20.35}$ Although it seems like the predicted sodiation/desodiation mechanism is the

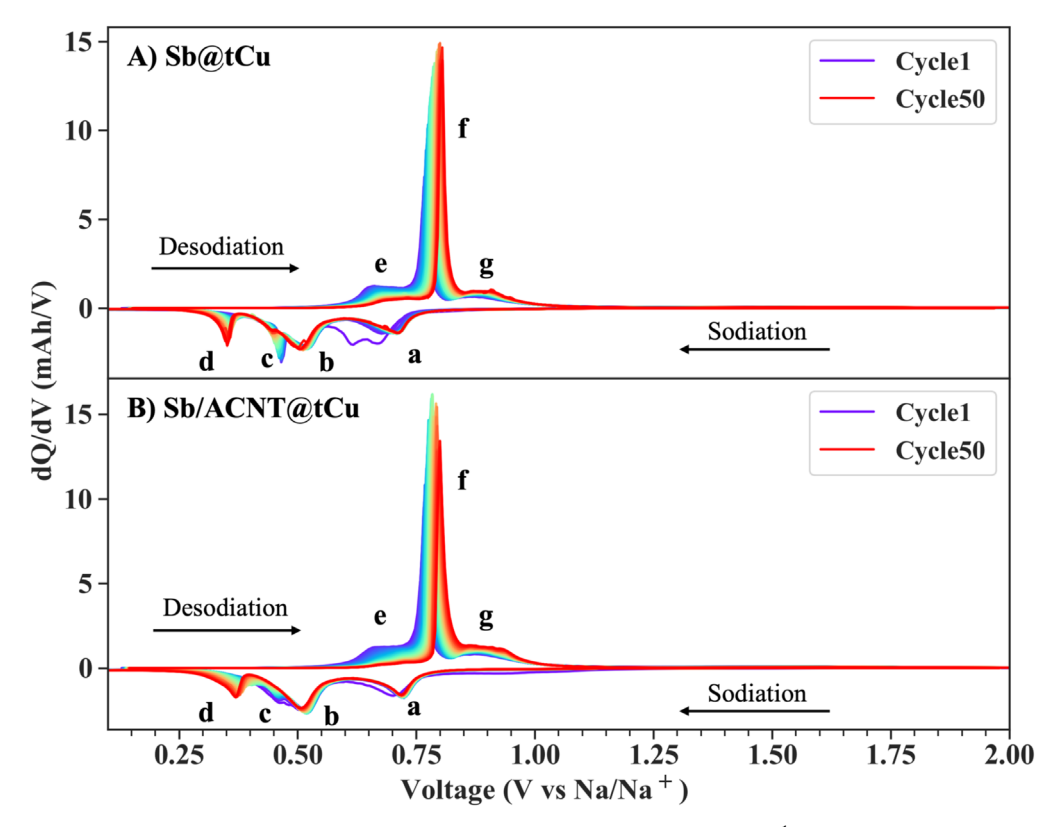


Figure 6. Differential capacity plots for both Sb@tCu (A) and Sb/ACNT@tCu (B) cycled at 0.1 mA mg⁻¹ in a Na-ion half-cell.

same in both Sb@tCu and Sb/ACNT@tCu, there are slight differences in the intensity of peak "c", and we have conducted several controls to verify that the electrochemical reactions present were inherent to the innate properties of Sb alone.

Influences of impurities and additives on electrodeposited Sb@tCu and Sb/ACNT@tCu composite films.—Incorporation of ACNTs in electrodeposited Sb films.—To further understand the sodiation process of Sb/ACNT, a few steps were taken back to solely investigate the sodiation of ACNT. The ACNT thin film was synthesized in a similar fashion as the electrodeposition of Sb/ACNT, except through electrophoretic methods. Using electrophoresis, the positively charged ACNTs were attracted to the negatively biased textured Cu foil and adhered to the surface. To verify that ACNTs were well adhered to the surface of the textured Cu, SEM was conducted. By characterizing the films with SEM, Fig. 7, it was observed that ACNTs were well dispersed throughout the film and were well adhered even after washing the film. The even dispersion of ACNT was characterized by the web-like features on the textured Cu foil. All cycling parameters were the same as the electrodeposited films to reproduce a similar electrochemical environment. The DCA plot, seen in Fig. 7, verifies that while ACNTs do have some electrochemical activity during the first cycle, all consecutive cycles show a very minimal contribution to the capacity, and it is concluded that ACNTs do not reversibly sodiate in this system.

Impact of Sb_2O_3 on electrodeposited Sb films.—To verify if other components of the electrodeposition solution were incorporated in the deposited film, XPS was used to characterize the environments present on the surface as well as throughout the film via sputtering. The Carbon 1s XPS spectra shown in Fig. 8 indicate that gluconate and CTAB are not significantly included in the electrodeposited films. This is shown by the argon sputtering of the Sb@tCu film not having any carbon signal after the initial adventitious carbon at \sim 285 eV is removed. The Sb/ACNT@tCu film has carbon present through different times of argon sputtering showing the inclusion of

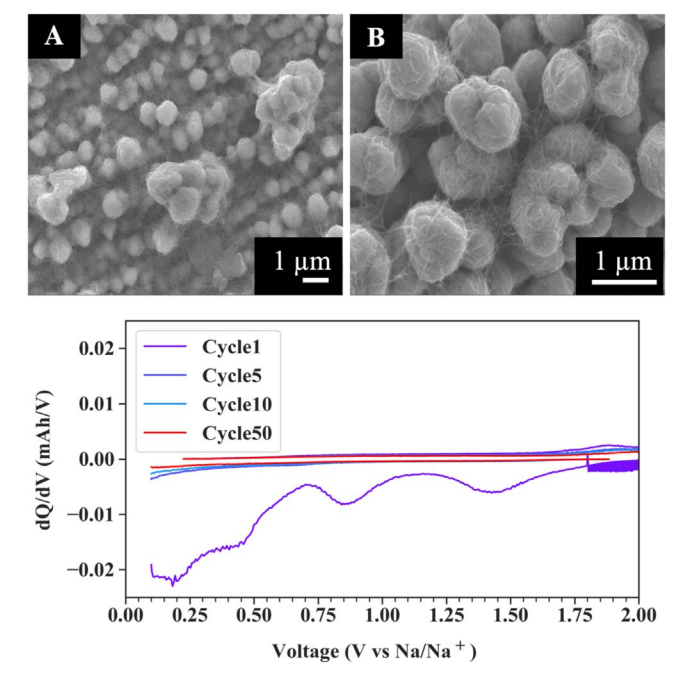


Figure 7. SEM images ACNTs electrophoretically deposited on tCu (A)–(B). Differential capacity plot of ACNT@tCu cycled in a Na-ion half-cell at $0.1~\text{mA}~\text{mg}^{-1}$ in 1M NaPF $_6$ in EC:DEC:DMC with 5% FEC (C).

the ACNTs into the film. It is hypothesized that the carbon peak is shrinking over sputter time because the ACNTs sputter away faster than the Sb film. Although electrodeposited Sb films don't include a significant amount of solution additives incorporated in the film, the main impurity present is the incorporation of Sb₂O₃. Through XPS, shown in Fig. 8, Sb₂O₃ 3/2 and 5/2 can be seen on the surface of

Table I. Hypothesized reactions occurring	g for the sodiation/desodiation of Sb anodes in Na-ion half-cells after cy	ycle 1 based on work by Allan et al. $(0.4 < x < 0.5)$.

	Sodiation Reactions (Charging)		_	Desodiation Reactions (Discharging)		
	Reaction	V vs Na/Na ⁺		Reaction	V vs Na/Na ⁺	
a	$Na_{1.0}Sb + Sb + Na^+ \rightarrow Na_{1.7}Sb + Sb$	0.70 V	e	Na_3Sb (cub & hex) $\rightarrow Na_{1.7}Sb + Na_3Sb$ (cub & hex) $+ Na^+$	0.65 V	
b	$\mathrm{Na_{1.7}Sb} + \mathrm{Sb} + \mathrm{Na^+} ightarrow \mathrm{Na_{1.7}Sb} + \mathrm{Na_{3-x}Sb}$	0.50 V	f	Na_3Sb (cub & hex) + $Na_{1.7}Sb \rightarrow Na_{1.0}Sb + Na^+$	0.77 V	
c	$Na_{1.7}Sb + Na_{3-x}Sb + Na^+ \rightarrow Na_{3-x}Sb + Na_3Sb$ (cub & hex)	0.47 V	g	$Na_{1.0}Sb \rightarrow Na_{1.0}Sb + Sb + Na^+$	0.85 V	
d	$Na_{3-x}Sb + Na_3Sb$ (cub &hex) $+ Na^+ \rightarrow Na_3Sb$ (cub & hex)	0.36 V				

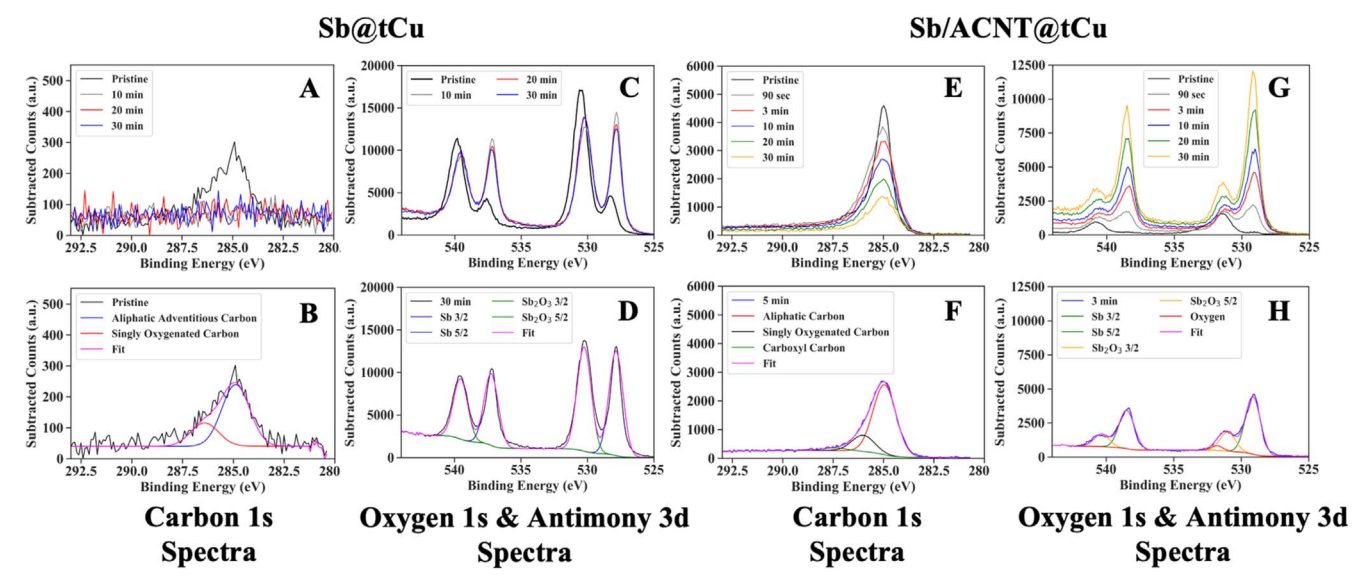


Figure 8. XPS of Sb@tCu (left) with the carbon 1s (A,B) and oxygen 1s and antimony 3d spectra (C,D) at different sputtering times. XPS of Sb/ACNT@tCu (right) with the carbon 1s (E,F) and oxygen 1s and antimony 3d spectra (F,H) at different sputtering times. The top row of spectra depict the raw data while the bottom row show the same data with fits.

both Sb@tCu and Sb/ACNT@tCu films at 540 and 531 eV respectively. While the Sb⁰ concentrations increased as a function of sputter time (Sb 3d 3/2 and 5/2: 537 and 528 eV), oxides are present throughout the bulk of the electrode and the conversion reaction of Sb + Na₂O \rightarrow Sb₂O₃ can be seen through the DCA shown in Fig. 9B. Although oxides are considered impurities in this study, Sb₂O₃ anodes have been examined for Na-ion battery applications and its inclusion in Sb films has previously been investigated. The inclusion of Sb₂O₃ has been seen to be beneficial in terms of capacity and possibly lifetime in other reports,

however, our studies focus on understanding the sodiation mechanism of Sb alone.

To control and understand the impact of Sb_2O_3 on the reaction mechanism of Sb, we wanted to control or eliminate the presence of Sb_2O_3 in the electrodeposited films. Because these films are deposited in aqueous solutions, in air, it is difficult to control the formation of oxides through this synthetic method and reagents used. Through various studies, researchers have found that the conversion of Sb_2O_3 to Sb and Na_2O occurs at $\sim 1.0~V~vs~Na/Na^+$ and the reformation of Sb_2O_3 from Sb and Na_2O occurs from 1.5-2.5~V~vs

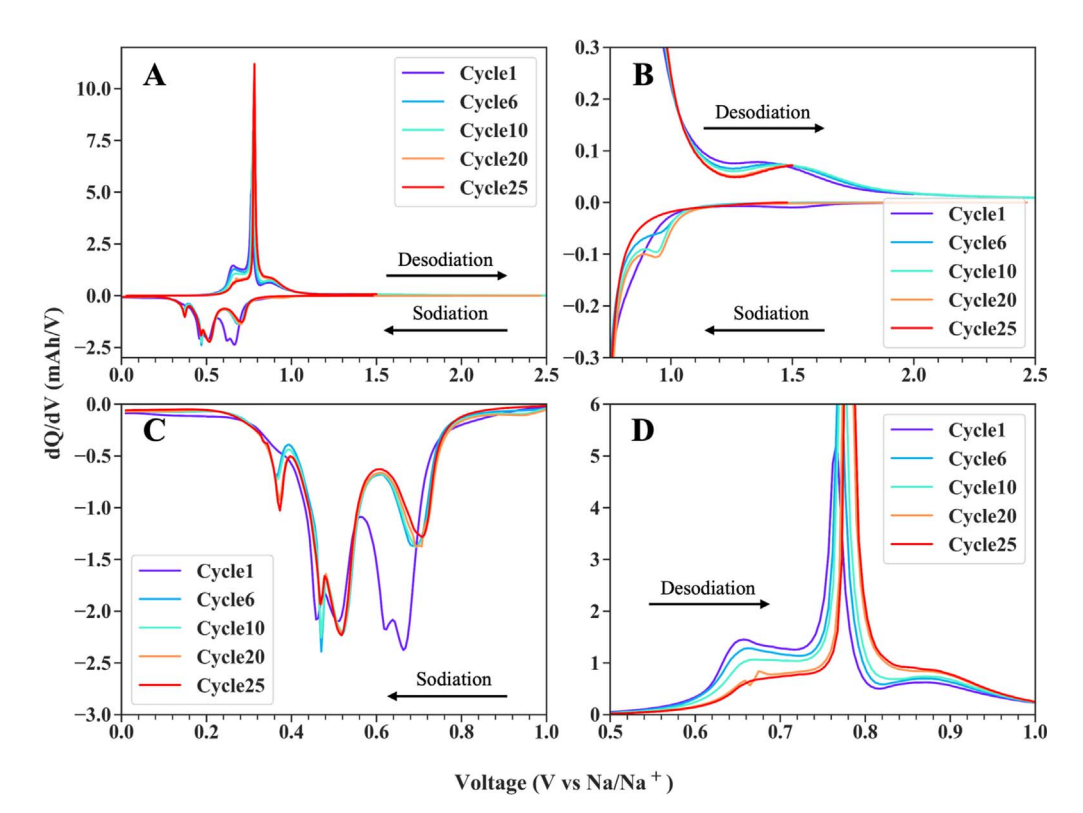


Figure 9. Differential capacity plots for Sb@tCu cycled in a Na-ion half-cell cycled at 0.1 mA mg⁻¹. (A) demonstrates the complete sodiation/desodiation reactions occurring. While (B) shows a zoomed in look at the conversion of Sb to Sb₂O₃, (C) only shows the sodiation reactions, and (D) shows the desodiation reactions in more detail.

Table II. Voltage limits for the three conditions tested to control the conversion reactions related to Sb_2O_3 .

Condition	Voltage Limits (V vs Na/Na ⁺)	Cycles
1	0.01–2.0 V	1–6
2	0.01-2.5 V	7-20
3	0.01-1.5 V	21-25

Na/Na $^+$. To control the presence of Sb₂O₃ cycling conditions were varied for the same Sb@tCu film in a Na-ion half-cell, Table II. The voltage window was varied between three different conditions described in Table II. The first condition cycled the cell at a constant current (0.1 mA mg $^{-1}$) from 0.01–2.0 V vs Na/Na $^+$ (regular cycling conditions), then the voltage window was extended to 2.5 V vs Na/Na $^+$ (Condition 2) to allow for the "complete" conversion of Sb and Na₂O to Sb₂O₃. By extending the upper voltage limit it can be seen in the DCA, shown in Fig. 9, that the conversion reaction from Sb₂O₃ to Sb and Na₂O at 1.0 V vs Na/Na $^+$ has increased and supports the hypothesis that extending the upper voltage limit does introduce more Sb₂O₃.

The third and final condition decreases the upper voltage limit to 1.5 V vs Na/Na⁺ to allow for the complete desodiation of Sb but also prevents the full conversion of Na₂O and Sb to Sb₂O₃. Cycle 22 represents the third cycling condition and the conversion of Sb₂O₃ to Sb at 1.0 V vs Na/Na⁺ which decreased significantly. Lowering the upper voltage limit decreases the amount of Sb₂O₃ and provides control on the impact Sb₂O₃ has on the reaction mechanism of electrodeposited Sb films. These voltage control experiments were also conducted on Sb/ACNT@tCu, and similar trends in controlling Sb₂O₃ inclusion can be seen in Fig. S5. Throughout these three cycling conditions the reactions corresponding to the sodiation/ desodiation of Sb slightly vary, where peak "a" is influenced by the additional conversion of Sb₂O₃ to Sb, and the intensity of the peak remains the same from cycles 6-20 and are not brought down by the loss of active material. Peaks "b" and "c" remain unchanged and are thought to be influenced by the previously described degradation mechanism for Sb films. Other significant changes are seen in peak "d", where the peak increases over cycling. Although this is also a

trend when the cell is normally cycled from 0.01-2 V. As previously mentioned, we hypothesized that the fourth reaction could be due to kinetic limitations shifting the reactions occruing in peak "c" to overpotentials. These reactions are associated to the formation of the fully sodiated hexagonal Na₃Sb phase, and the possible formation of the metastable cubic Na₃Sb phase that has been seen in other studies and has been synthesized through solid state methods under elevated pressures. 44 The increase in intensity of peak "d" could be due to the additional volume expansion that occurs from the inclusion of unreacted Sb₂O₃ leading to the additional formation of the metastable phase. In addition, increasing the amount of Sb₂O₃ is shown to increase the capacity of both Sb@tCu and Sb/ACNT@tCu in cycles 10 and 20, and the capacity is reduced when the Sb₂O₃ conversion reactions are cut off in cycle 25, seen in the voltage profiles in Figs. S6 and S7 for the Sb@tCu and Sb/ACNT@tCu films, respectively. Overall, these cycling conditions demonstrate the ability to "control" the concentration of Sb₂O₃ in the film and its effects on the reaction mechanism of Sb sodiation/desodiation.

Characterization of slurry casted Sb composite films.—To investigate if fabrication methods have a significant influence on the electrochemical reactions of Sb, we fabricated Sb composite films through the commonly used slurry casting method. The slurry casting method typically involves the grinding of active material (Sb), a conductive additive (Super P), and polymeric binder (PVDF, PAA, CMC) at different weight ratios. Then a wetting solvent (NMP, water) is introduced to create a viscous film that can then be cast onto a current collector. Several studies have investigated how different binders and additives can optimize mechanical integrity and rate capabilities, but few have investigated how the electrochemical reactions of the active material in question are directly influenced by these additives. 33,49–55

Two different Sb composites were fabricated through the slurry casting method using two commonly used binders, PAA and CMC, and Super P as the conductive additive. All slurries were made with a ratio of 70:15:15 wt% of active material, binder, and conductive additive. SEM images, shown in Fig. 10, show a homogenous mixture and dispersion of Sb particles throughout the film that are coated in binder and conductive additive. Some cracks are seen in the CMC-based slurry, but good adhesion onto the tCu foil was

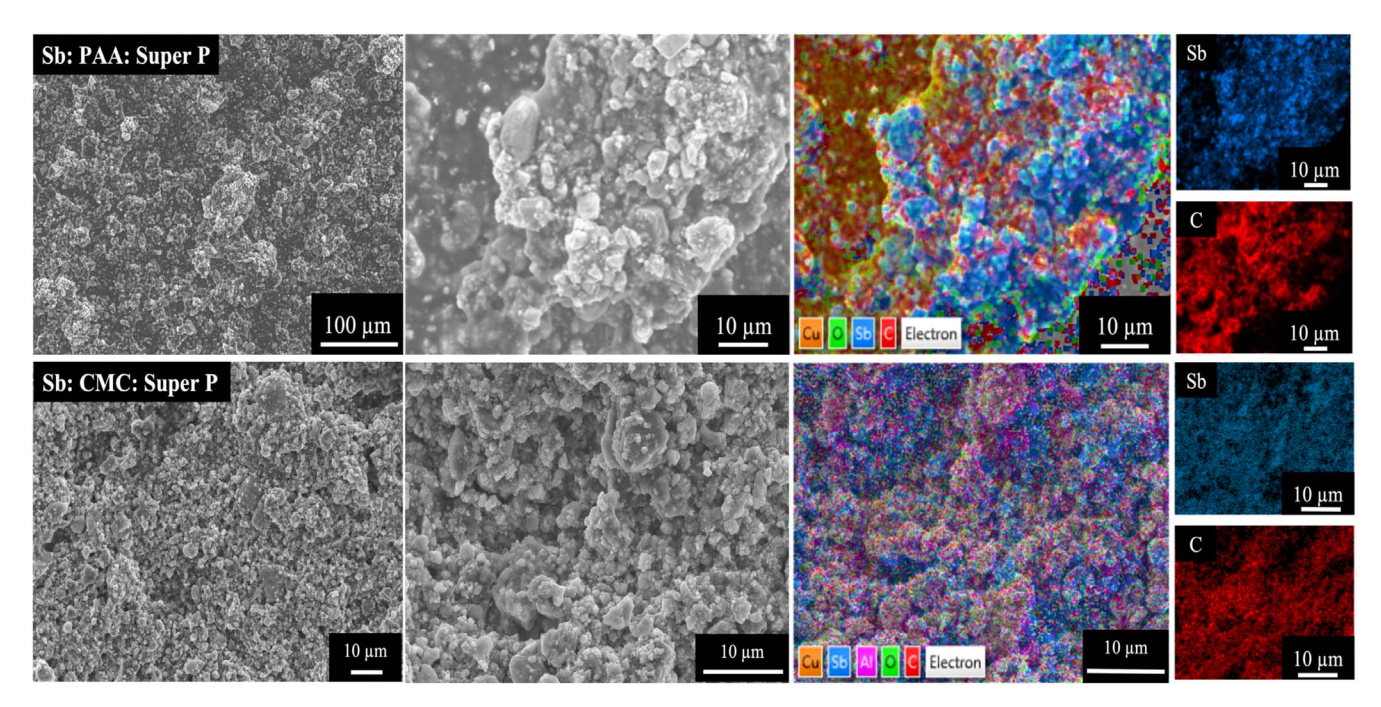


Figure 10. SEM images and EDS maps of slurry casted Sb films consisting of Sb:PAA: Super P and Sb:CMC:Super P. Full EDS maps of the Sb:CMC:Super P film are included in Fig. S9.

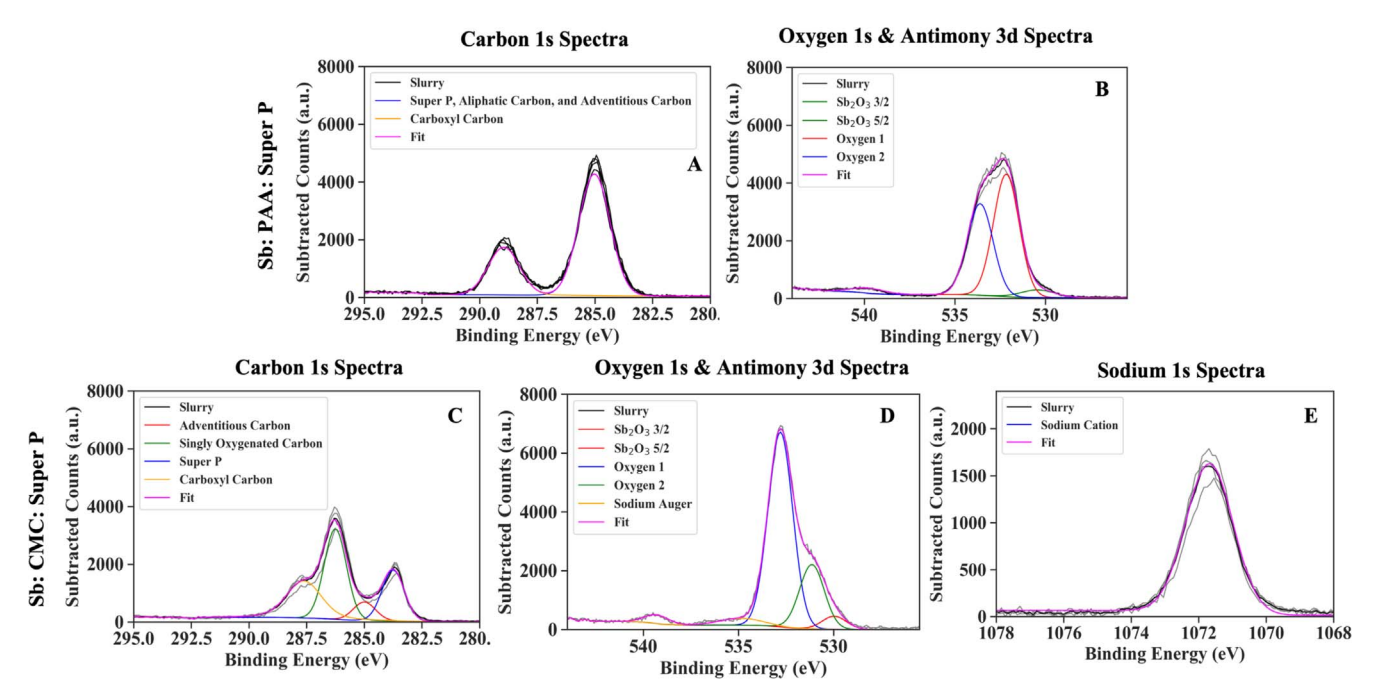


Figure 11. Fitted XPS of the Sb:PAA:Super P slurry with carbon 1s (A) and oxygen 1s and antimony 3d environments (B). Fitted XPS of the Sb:CMC:Super P slurry with carbon 1s (C), oxygen 1s and antimony 3d (D) and sodium 1s (E) spectra.

apparent when the films were punched out of the foil and no delamination occurred (Fig. S11). Oxygen is also incorporated in the film and is concentrated on the surface of the Sb particles shown through EDS in Fig. 10. The inclusion of Sb₂O₃ 3/2 is minimal at 540 eV in comparison to the electrodeposited films and no Sb⁰ is present as seen through XPS in Fig. 11. The limited amount of Sb present means that the components of the slurry cover up the antimony particles. The majority of the XPS signal is comprised of the slurry environments. For PAA the carbon and oxygen environments match the O=C and O-C poly carboxyl functional groups of the binder. Na CMC also has appropriate O-C and CO₂ ratios in the carbon and oxygen XPS. XPS also shows the inclusion of sodium cations in the CMC due to the use of the Na CMC salt. To attempt to deconvolute the chemical environments of the slurry by XPS, Na CMC, PAA, and Super P were analyzed individually, these XPS spectra with examples fitting can be found in Fig. S10. Previous work from our group further details how our XPS data is analyzed and fitted. 56,57 Calibration for XPS spectra of slurry casted films is a complicated process as the adventitious aliphatic carbon, which is often used as a self-consistent calibration peak, is difficult to identify in slurry casted films with conductive carbon additives like Super This means that clear identification of the starting chemical environments on the surface is challenging and deconvolution of the SEI formed during cycling is nearly impossible.

Using PXRD as a structural characterization method, Fig. 12, Sb in these slurry casted films is highly crystalline, and we attribute differences in the sodiation potentials of the initial sodiation of Sb in the first cycle to overpotentials needed to break down the crystalline Sb. 20,35 In addition, the size of the particles in these slurry composites vary in size from 1 to 10 μ m and are much larger than the electrodeposited Sb particles but have been significantly reduced from the pristine powder where the largest Sb particles were measured to be approximately 70 μ m as seen in the SEM images of the pristine Sb powder in Fig. S8. The difference in particle size can lead to issues with rate capability due to the longer solid-state diffusion distances the Na ion has to travel. To help reduce kinetic limitations all cells were cycled at 0.1 mA mg $^{-1}$.

Electrochemical performance of slurry Sb composite films in naion half-cells.—The electrochemical performance of the Sb:PAA: Super P and Sb:CMC:Super P slurries was tested by galvanostatically

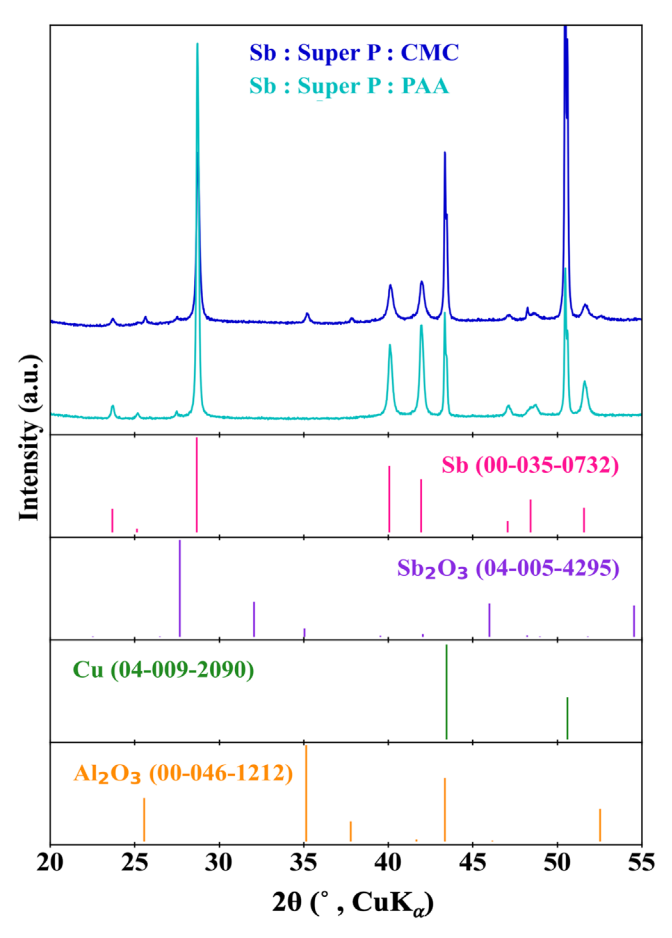


Figure 12. PXRD of the slurry casted Sb composites, Sb:PAA:Super P (blue), and Sb:CMC:Super P (cyan).

cycling the films in a Na-ion half-cell with the same electrolyte, and under the same cycling conditions as the Sb@tCu and Sb/ACNT@tCu electrodeposited films. The cycle lifetime and the capacity retention of

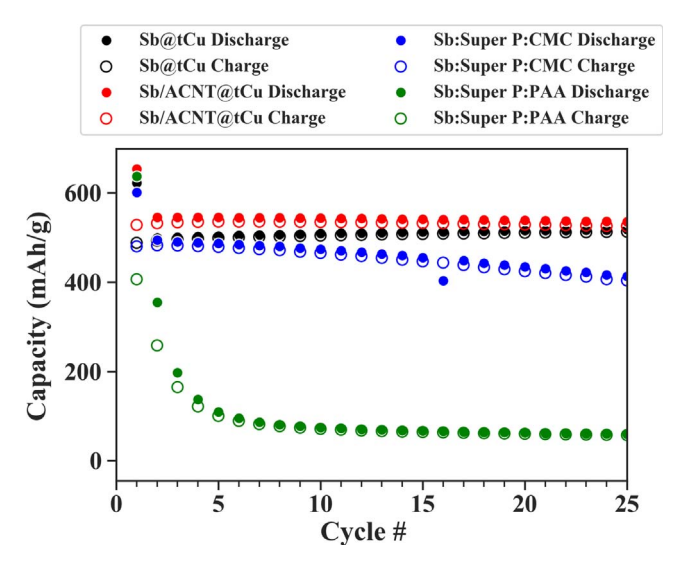


Figure 13. Specific capacity electrodeposited Sb@tCu and Sb/ACNT@tCu with the slurry casted Sb composites. All anode films were cycled in a Naion half-cell at 0.1 mA mg⁻¹.

the slurry casted films are shown in Fig. 13. Both slurry composites had poor cycle life in comparison to the electrodeposited films due to the instability of the slurry casted films. The Sb:PAA:Super P had a very rapid loss in capacity in early cycles and then stabilized at low capacities represented by delamination of the film from the current collector and/or excessive SEI formation. This delamination was witnessed when the cell was taken apart for ex situ studies. Initially,

both slurries had good adhesion as evidenced by very little delamination of the film when electrodes were punched out of the foil, Fig. S11. The poor capacity retention is thought to be related to volume expansion of the active material, along with the needed optimization of the electrolyte used. Other reports have reported longer lifetimes with similar composition and fabrication methods but could not be reproduced. Different electrolytes and cycling conditions may also be heavily influencing the performance of specific binders in these anode films. ^{33,49–51,55}

Influences of fabrication method on sodiation and desodiation pathway of Sb composite films.—Although the slurry casted films have short lifetimes, sufficient cycles were gathered to identify initial electrochemical reactions and how these reactions change over the lifetime of the cell. Initially, when plotting the DCA for the slurry casted films, the DCA showed what is commonly seen in the field, where the sodiation peaks "a-c" were present and peak "d" was drowned out by the intensity of the peaks around it, seen in Fig. S12. The drowning out of peak "d" is similar to the Sb₂O₃ conversion reactions discussed previously and demonstrates a need to carefully plot DCA plots at different voltages and intensities. Without careful plotting of DCA many sodiation/desodiation reactions could be ignored and the understanding of these processes would be incomplete.

By taking a closer look at the DCA plots in Fig. 14, differences in the sodiation and desodiation reactions are present during initial cycles as well as in longer duration cycling studies, signifying that the initial reactions are occurring through different pathways. This indicates that these systems degrade differently. In both slurries, the first cycle is dominated by one reaction process at 0.50 V and 0.40 V vs Na/Na⁺, for the Sb:CMC:Super P and Sb:PAA:Super P, respectively. This process is representative of the initial breakdown

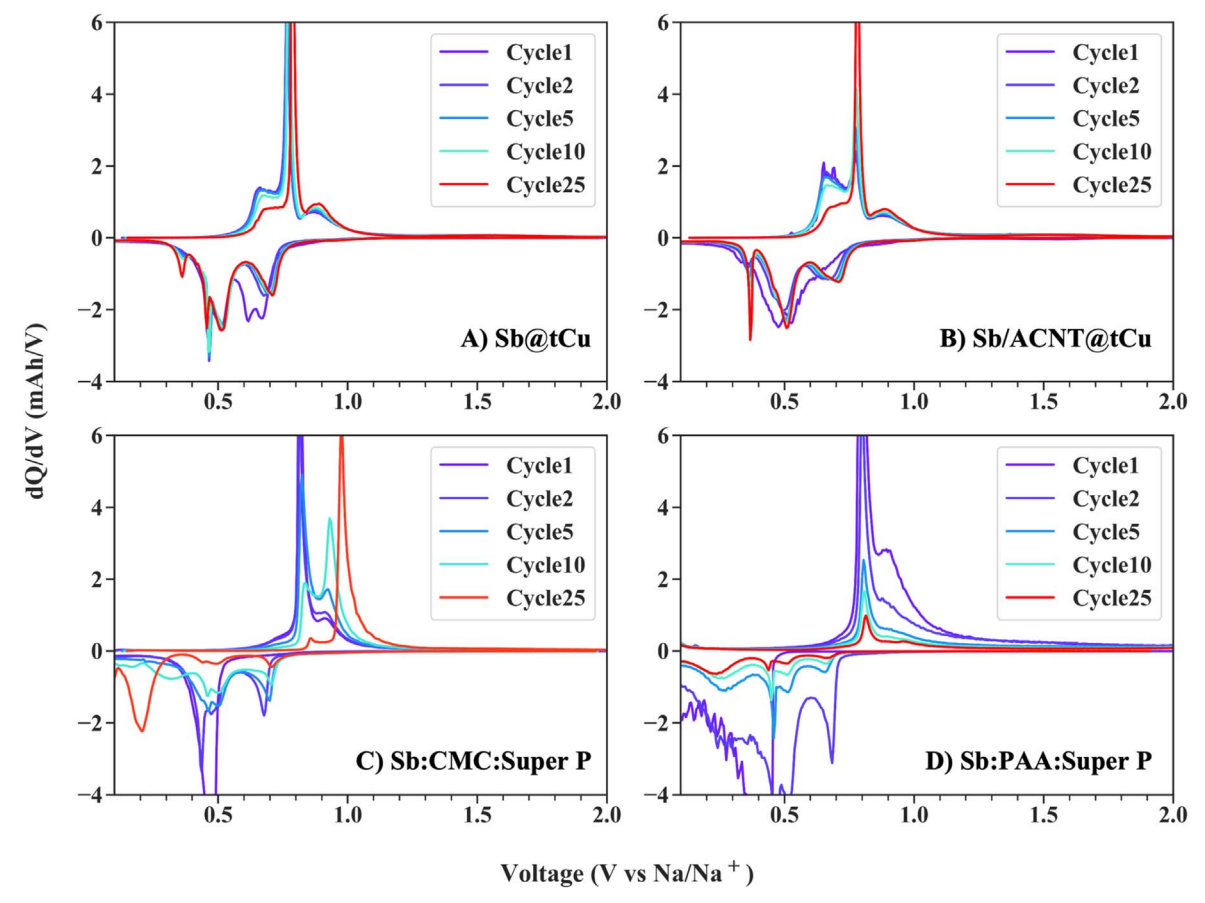


Figure 14. Differential capacity plots for electrodeposited Sb@tCu (A), and Sb/ACNT@tCu (B), and slurry casted Sb:CMC:Super P (C), and Sb:PAA: Super P (D). All anodes were cycled in a Na-ion half-cell cycled at 0.1 mA mg⁻¹.

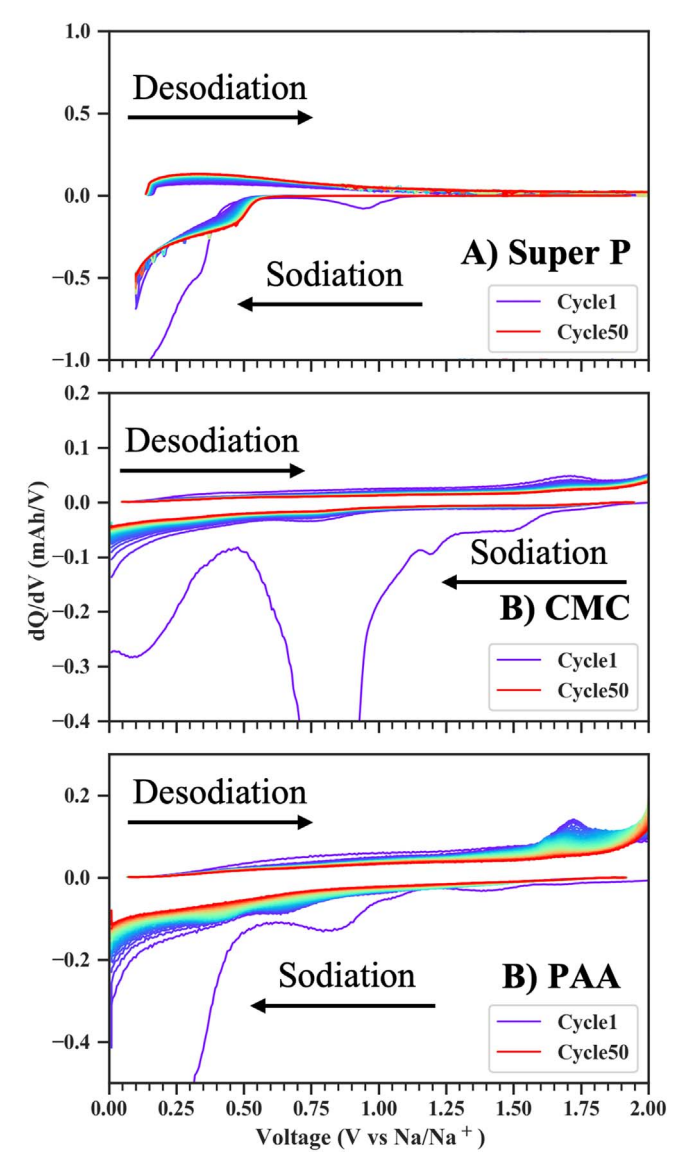


Figure 15. DCA plots of slurry casted controls. A 50/50 wt% composite of Super P and PAA (a), a 100 wt% PAA composite (b), and a 100 wt% CMC composite (c). All cells were cycled at 0.1 mA mg⁻¹ in a Na-ion half-cell.

and sodiation of crystalline Sb.²⁰ Upon later cycles, this single process separates to form multistep processes that resemble the sodiation processes in the electrodeposited films. For the sodiation reactions in the slurry casted films, peaks "a-c" can be identified clearly after the initial cycle, and the potentials at which they occur closely match the potentials for the electrodeposited films. One significant difference to note is peak "d", where this reaction occurs soon after peak "c" at ~0.36 V vs Na/Na⁺ in the electrodeposited films. Peak "c" is related to the full sodiation of the electrode from Na_{3-x}Sb to crystalline cubic and hexagonal Na₃Sb. In the slurry casted films, it is apparent that this reaction is shifted to considerable overpotentials and has significantly broadened when compared to the electrodeposited films. The shift in overpotential and peak broadening are representative of kinetic limitations such as sluggish Naion diffusion. A similar process occurs in the electrodeposited films over cycles as peak "c" decreases and peak "d" increases sharply signifying that the final sodiation reaction becomes kinetically limited over time. These differences in kinetic limitations may arise from how these films were fabricated.

These slurry casted films consist of Sb particles coated with conductive carbon imbedded in a polymer binder matrix as seen in the SEM and EDS maps in Fig. 10. When compared to the electrodeposited films, the Sb particles are not as densely packed in the film, also shown by the lack of strain in the PXRD in Fig. S4. This difference in packing may influence the diffusivity of sodium in the film and allow for the final sodiation reaction to occur at lower overpotentials. This influence of strain and dense Sb packing is also hypothesized to impact the first desodiation reaction represented by peak "e" in Figs. 6 and 14 at 0.65 V. In the DCA plots in Fig. 14, it appears that peak "e" is not present or has been shifted to overpotentials represented by the increase in intensity and broadening of peak "f". The densely packed electrodeposited films allow for facile Na⁺ diffusion to form the Na_{3-x}Sb phase at less positive voltage potentials.

In addition, these slurry composites contain polymeric binders and conductive additives that may reversably sodiate and contribute to the reactions present in the DCA plots. To determine if these reactions are related to the final sodiation of Sb or the components of the composite, several controls were conducted on the individual components of the slurry. To test if the conductive additive had a significant influence on the electrochemical reactions a composite was casted composed of a 50:50 wt% of Super P: PAA. In addition, PAA and CMC were casted onto tCu by suspending the individual binders in their respective solvent and creating a viscous mixture. These controls were galvanostatically cycled under the same cycling parameters previously mentioned and with the same electrolyte. In the DCA plot of Super P in Fig. 15A, it is shown that Super P does sodiate at a range from 0.50-0.10 V vs Na/Na⁺. This reaction appears to be slightly reversible and is due to the storage of sodium in graphite interlayers. These results are validated by other studies that also report the sodiation of Super P. ^{59,60} The sodiation of Super P at these potentials could be the identity of the broad final sodiation peak at ~0.5 V vs Na/Na⁺ in both Sb:CMC:Super P and Sb:PAA: Super P composites. The DCA plots of PAA and CMC, shown in Figs. 15B and 15C, show that the binders do not sodiate but are electrochemically active in the electrolyte used. In cycle 1, both binders exhibit electrochemical reactions that could be from the initial formation of SEI through the reduction of the electrolyte. These findings testify to the complexity that arises from the inclusion of conductive additives and binders in slurry composites. This complexity can lead to the misidentification of electrochemical processes and can inhibit the understanding of the sodiation/ desodiation reactions for electrode materials.

Conlusions

To aid in the fundamental understanding of the complex sodiation/ desodiation mechanism of Sb in Na-ion cells, we have described the impact film composition and fabrication methods have on the electrochemical reactions present while cycling. In this study, the analysis of cycling performance and DCA plots showed that the sodiation of Sb is complex and can easily be influenced by the composition of the film. In slurry casted Sb composites, the lifetime was significantly shorter due to delamination and pulverization of the film and possibly an increase in the SEI. Although the lifetime was short the reaction mechanism was still analyzed for the first 25 cycles through DCA, and significant differences were noted between the slurry casted composites and the electrodeposited films. The slurry composite films consisted of large, dispersed Sb particles, a carbon conductive additive (Super P), and a polymeric binder (CMC or PAA). Through these studies, it was confirmed that Super P does sodiate and complicates the accurate assignment of reactions at specific voltages. In addition, the polymeric binders were seen to be electrochemically active and decomposed into the SEI during the first cycle, leading to additional polarization of the sodiation and desodiation of Sb.

In contrast, the electrodeposited Sb composites demonstrated how this fabrication technique allows for the control of particle size, morphology, porosity, and composition. Through electrodeposition, Sb is well adhered to the current collector and allows for longer cycle life. In addition, this technique allows for the co-deposition of Sb with conductive additives (ACNTs), while preventing other complexing agents in solution from depositing, allowing for a film mainly composed of Sb and/or Sb/ACNTs. Although Sb₂O₃ is incorporated in these films, it was demonstrated that conversion reactions of Sb₂O₃ can easily be separated from Sb, and the voltage window for cycling these cells can be modified to prevent the conversion of Sb to Sb₂O₃. Through DCA, hypothesized reactions could be assigned without convolution from additives and binders as ACNTs do not sodiate. When comparing the DCA of electrodeposited and slurry casted composites, significant differences were noted in the final sodiation reaction and the first desodiation reaction. These reactions are always present in the electrodeposited films examined in this study and are rarely reported in the literature. Although the slurry casted films show some activity at lower potentials, it is difficult to accurately determine what reactions are occurring due to the composition of the films and the complications due to binders. The final sodiation reaction is hypothesized to be the final conversion to Na₃Sb and is kinetically limited to varying degrees due to the method in which the electrode was fabricated. Additionally, we hypothesize that the final sodiated hexagonal Na₃Sb phase may be accompanied by the metastable cubic phase due to increased strain within in the film caused by volume expansion that could create enough pressure to access the metastable phase. We hypothesize that the formation of the metastable cubic Na₃Sb phase may be present in our electrodeposited films due to the dense packing of Sb particles, where the volume expansion upon sodiation may lead to sufficient pressure within the film to allow access to the metastable phase.

Overall, these studies have demonstrated the viability of electrodeposition as a fabrication method, and how it can provide significant control on the composition, and morphology, of the film. This synthetic control can lead to the detailed, systematic investigation of the sodiation/desodiation reaction mechanisms and other parameters, such as electrolyte composition, and SEI studies, without having to worry about the influences of binders and other conductive additives. These studies and fabrication technique will not only benefit Sb-based anodes but will also lead to better fundamental studies and processing of anode materials and electrolytes for lithium and beyond lithium technologies.

Acknowledgments

This work was partially funded by NSF SSMC-1710672. Special thanks to the Analytical Resources Core staff at Colorado State University, especially Dr. Patrick McCurdy and Dr. Rebecca Miller for their help with XPS, SEM, and EDS.

ORCID

Kelly Nieto https://orcid.org/0000-0002-8833-0113 Nathan J. Gimble https://orcid.org/0000-0003-0816-5291 Amanda R. Kale https://orcid.org/0000-0003-2058-902X Amy L. Prieto https://orcid.org/0000-0001-9235-185X

References

- 1. L. Li, Y. Zheng, S. Zhang, J. Yang, Z. Shao, and Z. Guo, Energy Environ. Sci., 11, 2310 (2018).
- 2. H. S. Hirsh, Y. Li, D. H. S. Tan, M. Zhang, E. Zhao, and Y. S. Meng, Adv. Energy Mater., 10, 32 (2020).
- 3. M. Sawicki and L. L. Shaw, RSC Adv., 5, 53129 (2015).
- 4. S. Liang, Y. J. Cheng, J. Zhu, Y. Xia, and P. Müller-Buschbaum, Small Methods, 4, 2000218 (2020).
- 5. A. Darwiche, C. Marino, M. T. Sougrati, B. Fraisse, L. Stievano, and L. Monconduit, J. Am. Chem. Soc., 134, 20805 (2012).
- 6. J. He, Y. Wei, T. Zhai, and H. Li, Mater. Chem. Front., 2, 437 (2018).
- 7. M. C. Schulze, R. M. Belson, L. A. Kraynak, and A. L. Prieto, Energy Storage Mater., 25, 572 (2019), In Press.
- H. Liu, Z. Wang, Z. Wu, S. Zhang, S. Ge, P. Guo, M. Hua, X. Lu, S. Wang, and J. Zhang, J. Alloys Compd., 833, 155127 (2020).
- Y. Yuan, S. Jan, Z. Wang, and X. Jin, J. Mater. Chem. A, 6, 5555 (2018).
- 10. Y. Zhu, X. Han, Y. Xu, Y. Liu, S. Zheng, K. Xu, L. Hu, and C. Wang, ACS Nano, 7, 6378 (2013).

- 11. R. Dugas, A. Ponrouch, G. Gachot, R. David, M. R. Palacin, and J. M. Tarascon, J. Electrochem. Soc., 163, A2333 (2016).
- 12. X. Bian, Y. Dong, D. Zhao, X. Ma, M. Qiu, J. Xu, L. Jiao, F. Cheng, and N. Zhang, ACS Appl. Mater. Interfaces, 12, 3554 (2020).
- 13. L. Bodenes, A. Darwiche, L. Monconduit, and H. Martinez, J. Power Sources, 273, 14 (2015)
- 14. L. Baggetto, P. Ganesh, C.-N. Sun, R. A. Meisner, T. A. Zawodzinski, and G. M. Veith, J. Mater. Chem. A, 1, 7985 (2013).
- 15. L. Ji et al., Adv. Mater., 26, 2901 (2014).
- 16. M. Sauban Ere, B. Yahia, F. Ed Eric Lemoigno, and M.-L. Doublet, J. Power Sources, 280, 695 (2015).
- 17. R. Caputo, Electron. Mater., 45, 999 (2016).
- J. S. Gutierrez-Kolar, L. Baggetto, X. Sang, D. Shin, V. Yurkiv, F. Mashayek, G. M. Veith, R. Shahbazian-Yassar, and R. R. Unocic, ACS Appl. Energy Mater., 2,
- 19. L. Baggetto, H.-Y. Hah, J.-C. Jumas, C. E. Johnson, J. A. Johnson, J. K. Keum, C. A. Bridges, and G. M. Veith, *J. Power Sources*, **267**, 329 (2014).
- 20. P. K. Allan, J. M. Griffin, A. Darwiche, O. J. Borkiewicz, K. M. Wiaderek, K. W. Chapman, A. J. Morris, P. J. Chupas, L. Monconduit, and C. P. Grey, J. Am. Chem. Soc., 138, 2352 (2016).
- 21. W. Ma, J. Wang, H. Gao, J. Niu, F. Luo, Z. Peng, and Z. Zhang, *Energy Storage* Mater., 13, 247 (2018).
- 22. B. Kong, L. Zu, and C. Peng, J. Am. Chem. Soc., 50, 16533 (2016).
- 23. H. Zhang, W. An, H. Song, B. Xiang, S. Mei, Y. Hu, and B. Gao, Solid State Ionics, **352**, 115365 (2020).
- 24. L. Liang, Y. Xu, C. Wang, L. Wen, Y. Fang, Y. Mi, M. Zhou, H. Zhao, and Y. Lei, Energy Environ. Sci., 8, 2954 (2015).
- 25. Z. Li, X. Tan, P. Li, P. Kalisvaart, M. T. Janish, W. M. Mook, E. J. Luber, K. L. Jungjohann, C. B. Carter, and D. Mitlin, Nano Lett., 15, 6339 (2015).
- 26. Y.-S. Choi and J.-C. Lee, J. Mater. Chem. A, 7, 23121 (2019).
- 27. Y.-S. Choi and J.-C. Lee, *Electrochim. Acta*, 328, 135106 (2019).
- C. Liu, Z. G. Neale, and G. Cao, *Mater. Today*, 19, 109 (2016).
 C. Liu, Z. G. Neale, and G. Cao, *Mater. Today*, 19, 109 (2016).
 C. M. Wu, P. I. Pan, Y. W. Cheng, C. P. Liu, C. C. Chang, M. Avdeev, and S. K. Lin, J. Power Sources, 340, 14 (2017).
- 30. V. M. Nagulapati, Y. H. Yoon, D. S. Kim, H. Kim, W. S. Lee, J. H. Lee, K. H. Kim, J. Hur, I. T. Kim, and S. G. Lee, J. Ind. Eng. Chem., 76, 419 (2019).
- 31. V. M. Nagulapati, D. S. Kim, J. Oh, J. H. Lee, J. Hur, I. T. Kim, and S. G. Lee, Nanomaterials, 9, 1 (2019).
- 32. M. J. Piernas-Muñoz, E. Castillo-Martínez, J. L. Gómez-Cámer, and T. Rojo, Electrochim. Acta, 200, 123 (2016).
- 33. L. O. Vogt, M. El Kazzi, E. Jämstorp Berg, S. Pérez Villar, P. Novák, and C. Villevieille, Chem. Mater., 27, 1210 (2015). 34. M. C. Schulze, R. M. Belson, L. A. Kraynak, and A. L. Prieto, Energy Storage
- Mater., 25, 572 (2020).
- 35. Y. Yang, X. Yang, Y. Zhang, H. Hou, M. Jing, Y. Zhu, L. Fang, Q. Chen, and X. Ji, J. Power Sources, 282, 358 (2015).
- 36. N. J. Gimble, K. Nieto, and A. L. Prieto, *Electrochem. Soc. Interface*, 30, 59 (2021).
- 37. J. Ma and A. L. Prieto, Chem. Commun., 55, 6938 (2019). 38. J. M. Mosby and A. L. Prieto, J. Am. Chem. Soc., 130, 10656 (2008).
- 39. E. D. Jackson and A. L. Prieto, ACS Appl. Mater. Interfaces, 8, 30379 (2016).
- 40. M. C. Schulze, R. K. Schulze, and A. L. Prieto, J. Mater. Chem. A, 6, 12708 (2018).
- 41. D. T. Sawyer, *Chem. Rev.*, **64**, 633 (1964).
- 42. J.-Y. Hwang, S.-T. Myung, and Y.-K. Sun, Chem. Soc. Rev., 46, 3529 (2017).
- 43. M. Dubarry, A. Devie, and B. Y. Liaw, J. Energy and Power Sources, 1, 242 (2014).
- 44. M. E. Leonova, I. K. Bdikin, S. A. Kulinich, O. K. Gulish, L. G. Sevast'yanova, and K. P. Burdina, *Inorg. Mater.*, 39, 332 (2003).
- 45. A. Beutl, D. Cupid, and H. Flandorfer, J. Alloys Compd., 695, 1052 (2017).
- 46. J. Pan, N. Wang, Y. Zhou, X. Yang, W. Zhou, Y. Qian, and J. Yang, Nano Res., 10, 1794 (2017).
- 47. X. Li, J. Qu, H. Xie, Q. Song, G. Fu, and H. Yin, *Electrochim. Acta*, 332, 135501
- 48. D. Li, D. Yan, J. Ma, W. Qin, X. Zhang, T. Lu, and L. Pan, Ceram. Int., 42, 15634 (2016).
- S. L. Chou, Y. Pan, J. Z. Wang, H. K. Liu, and S. X. Dou, Phys. Chem. Chem. Phys., 16, 20347 (2014).
- 50. C. Bommier and X. Ji, Small, 14, 1 (2018).
- 51. M. Dahbi et al., *Electrochem. Commun.*, 44, 66 (2014).
- 52. S. Komaba, Y. Matsuura, T. Ishikawa, N. Yabuuchi, W. Murata, and S. Kuze, Electrochem. Commun., 21, 65 (2012).
- 53. Q. Fan, W. Zhang, J. Duan, K. Hong, L. Xue, and Y. Huang, *Electrochim. Acta*, 174, 970 (2015).
- 54. K. Dai, H. Zhao, Z. Wang, X. Song, V. Battaglia, and G. Liu, J. Power Sources, 263, 276 (2014).
- 55. R. R. Li, Z. Yang, X. X. He, X. H. Liu, H. Zhang, Y. Gao, Y. Qiao, L. Li, and S. L. Chou, Chem. Commun., 57, 12406 (2021).
- 56. N. J. Gimble, L. A. Kraynak, J. D. Schneider, M. C. Schulze, and A. L. Prieto, J. Power Sources, 489, 229171 (2021).
- 57. L. A. Kraynak, J. D. Schneider, and A. L. Prieto, J. Phys. Chem. C, 124, 26083
- 58. G. Greczynski and L. Hultman, *Prog. Mater Sci.*, 107, 100591 (2020).
- 59. B. Peng, Y. Xu, X. Wang, X. Shi, and F. M. Mulder, Sci. China Physics, Mech. Astron., 60, 064611 (2017).
- 60. C. M. Wu, P. I. Pan, Y. W. Cheng, C. P. Liu, C. C. Chang, M. Avdeev, and S. K. Lin, J. Power Sources, 340, 14 (2017).